Calorimeter calibration of the ComPol CubeSat gamma-ray polarimeter

Ion Cojocari[a], Matthias Meier[b,h], Philippe Laurent[a], Adrien Laviron[c], Marco Arrigucci[e], Marco Carminati[e], Griseld Deda[e], Carlo Fiorini[e], Katrin Geigenberger[b,h], Cynthia Glas[b,h], Jochen Greiner[g], Peter Hindenberger[b,h], Pietro King[e], Peter Lechner[f], Martin Losekamm[b,h], Susanne Mertens[b,h,d], David Meßmann[b,h], Sebastian Rückerl[b,h], Lorenzo Toscano[e], Ulrich Walter[b,h], Michael Willers[b,h]

[a] *Université Paris Cité, Université Paris-Saclay, CEA, CNRS, AIM, Gif-sur-Yvette, 91191, France*
[b] *TUM, Garching, 85748, Germany*
[c] *Université Paris-Saclay, CNRS/IN2P3, IJCLab, Orsay, 91405, France*
[d] *Max-Planck-Institut für Physik, München, 80805, Germany*
[e] *Politecnico di Milano, Milano, 20133, Italy*
[f] *Semiconductor Laboratory of the Max Planck Society, München, 81739, Germany*
[g] *Max-Planck Institute for extraterrestrial Physics, Garching, 85748, Germany*
[h] *Excellence Cluster ORIGINS, Garching, 85748, Germany*

Abstract

ComPol is a proposed CubeSat mission dedicated to long-term study of gamma-ray polarisation of astrophysical objects. Besides spectral and timing measurements, polarisation analysis can be a powerful tool in constraining current models of the geometry, magnetic field structure and acceleration mechanisms of different astrophysical sources. The ComPol payload is a Compton telescope optimised for polarimetry and consists of a 2 layer stacked detector configuration. The top layer, the scatterer, is a Silicon Drift Detector matrix developed by the Max Planck Institute for Physics and Politecnico di Milano. The second layer is a calorimeter consisting of a $CeBr_3$ scintillator read-out by silicon photo-multipliers developed at CEA Saclay. This paper presents the results of the prototype calorimeter calibration campaign, executed in March 2022 at IJCLab Orsay and simulations of the expected performance of the polarimeter using updated performance figures of the detectors.

Keywords:
instrumentation, gamma ray, polarimetry, astrophysics, CubeSat, scintillator, SiPM

1. Introduction

CubeSats have quickly become an attractive option and enabled space access for smaller actors, be it hobbyists like universities and schools or countries with no major space sector. This is primarily due to reduced cost, less stringent quality assurance procedures and numerous launch opportunities. While first used as a good training option, developing small satellites has become an opportunity to deploy full fledged observation instruments as seen by multiple working astronomy missions covering the whole electromagnetic spectrum and the plethora of proposed missions from the scientific community [1].

ComPol is a planned 3U mission dedicated to long-term observation of Cygnus X-1 in the 20 keV-1 MeV energy range. The ComPol payload consists of a Compton polarimeter situated in the middle of the nano-satellite as seen in figure 1, at the end of a collimator represented in white. The instrument fits in 1U of a CubeSat and consists of two detectors working in coincidence, a Silicon Drift Detector array, developed at MPP, Munich in collaboration with Politecnico di Milano, and a Cerium

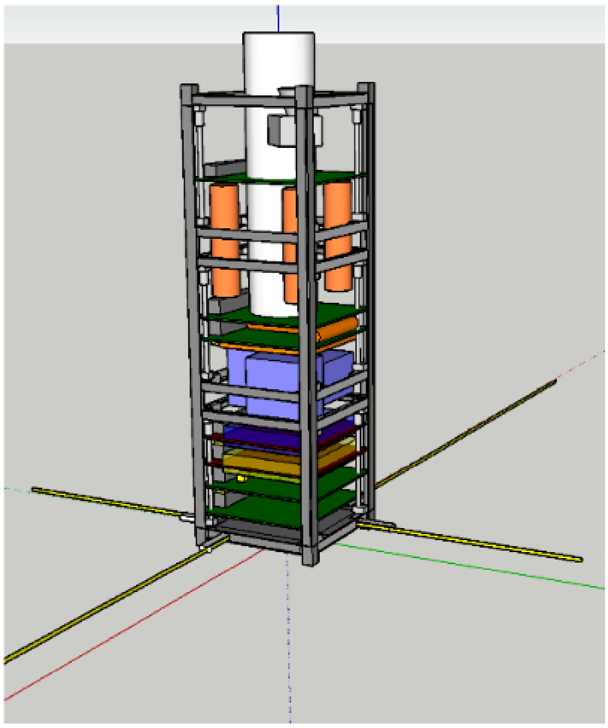

Figure 1: Preliminary design of the ComPol CubeSat.

Email address: ion.cojocari@cea.fr (Ion Cojocari)

Bromide scintillator read-out by silicon photo-multipliers coupled to an EASIROC ASIC [2], developed at CEA Saclay. A first prototype calorimeter has been developed in 2021 followed by extensive calibration campaigns. We have measured the energy response of the detector and evaluated the capacity to reconstruct the point-of-interaction inside the crystal.

2. Scientific context

Polarimetry could become the next tool in hard X-ray/gamma-ray astronomy. Although low flux levels and high background noise make polarimetric measurements quite challenging, they can provide key information on an astrophysical sources geometric configuration, magnetic field structure and high-energy emission mechanisms [3, 4]. Polarimetric measurements could shed a light on a plethora of high-energy sources characteristics which may not be accessible with currently used spectral or temporal analysis or imaging.

1. Polarimetry could reveal the processes at the heart of **Gamma-Ray Bursts (GRBs)** as well as the nature of the jets, the dissipation sites and radiation mechanism.
2. Polarimetric analysis of **pulsars** would let us probe the magnetic field structure, the particle acceleration and pair production processes in the magnetosphere as well as the gamma-ray emission mechanisms.
3. For **micro-quasars**, hard X-ray polarimetry can disentangle the jet emission from the disk photons scattered on thermal electrons thus probing the poorly known physics of the jets in the black hole vicinity.
4. Polarisation measurement can also be used to constrain current acceleration models for **solar flares** by measuring the pitch-angle distribution of the accelerated electrons impinging on the photosphere

This field has been gaining momentum the last decade with multiple flown balloon experiments like X-Calibur [5], PoGo [6], Phenex [7, 8], Ascot [9], Grips [10], GRAPE [11] and some satellite missions, which includes some that were not necessarily developed as polarimeters, like IBIS/INTEGRAL [12, 13], CZTI/AstroSAT [14] GAP/IKAROS [15] and POLAR on-board Tiangong-2 [16].

But for the time being, the only accepted space-telescope in the soft gamma-ray range with polarimetric capabilities is COSI [17], a NASA SMEX mission [18], that started as a balloon payload[19], scheduled for launch in 2025 which opens the possibility of joint observations of Cygnus X-1 with Com-Pol.

3. Compton polarimetry

Polarisation measurements of high energy photons rely on exploiting photon-matter interaction processes. In general, the three main effects : *photoelectric effect, Compton scattering and pair production* can be used in equivalent ways in order to measure the polarisation of the incoming photons. On the other hand, the detectors and subsequent data analysis will

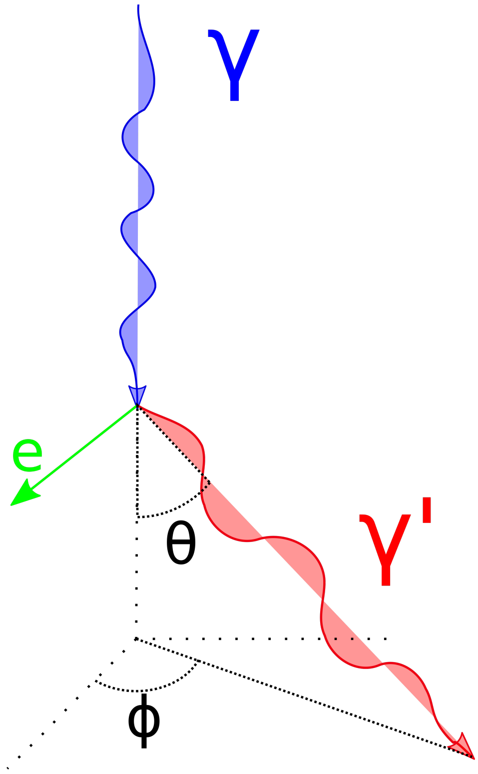

Figure 2: Compton scattering diagram with γ and γ' - the incident and scattered photon,respectively; θ - polar scatter angle and ϕ - azimuthal scatter angle.

vary greatly, depending on the exploited effect. The main constraint in instrument design is the energy band under observation. Thus, for the 10s of keV to 10 MeV energy band, the only feasible detection principle relies on Compton scattering since it is the predominant effect in this energy range.

$$E_{\gamma'} = \frac{E_\gamma}{1 + (E_\gamma/m_e c^2)(1 - \cos\theta)} \quad (1)$$

A traditional Compton telescope must have at least 2 detector planes working in coincidence. By exploiting the Compton scattering equation [20], it is possible to reconstruct both the origin ($\cos(\theta)$) and the energy (E_γ) of the incoming photon (see eq 1 and figure 2). In order to do so, both (or more) of the detection planes must be *imagers* and *spectrometers*. A Compton polarimeter will further exploit the azimuthal scatter angle of the photon to obtain information on the polarisation fraction (PF) and polarisation angle (PA). Indeed, the differential cross-section of the scattered photons is not isotropic, in polar or azimuthal directions, as described by the Klein-Nishina formula:

$$\frac{d\sigma}{d\Omega} = \frac{1}{2} r_e^2 \left(\frac{E_{\gamma'}}{E_\gamma}\right)^2 \left[\frac{E_\gamma}{E_{\gamma'}} + \frac{E_{\gamma'}}{E_\gamma} - 2\sin^2(\theta)\cos^2(\phi)\right] \quad (2)$$

Another critical point in the exploitation of polarimetry data are the systematics of the instrumental response. Indeed, the geometry of the detectors, pixel size and shape can create the illusion of a polarised signal where there is none. It is thus very

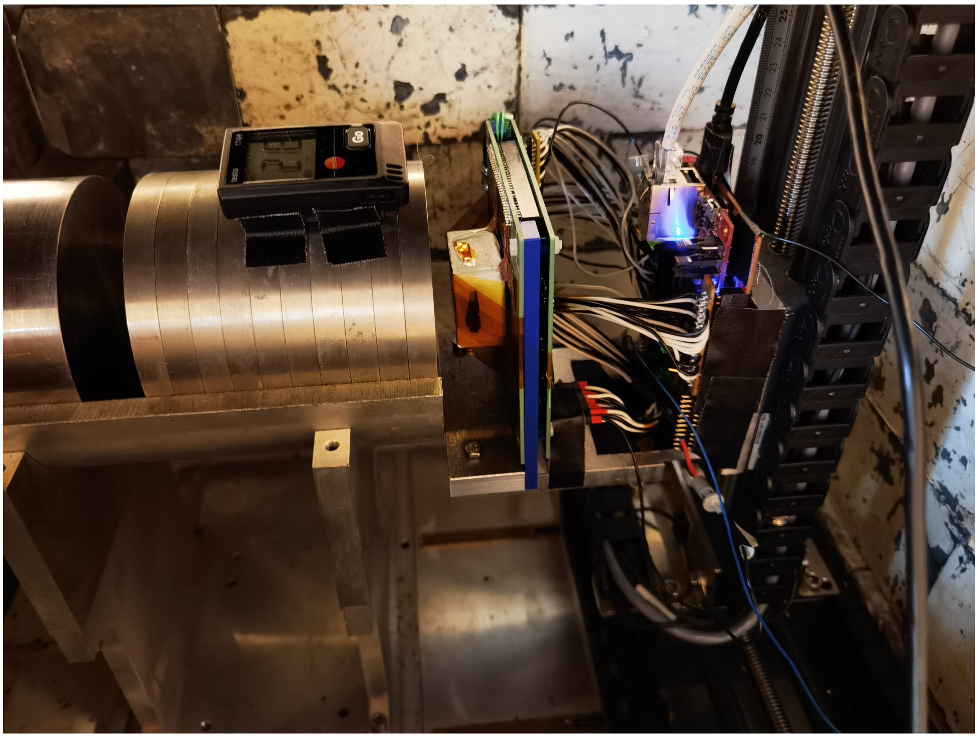

Figure 3: Photo of the setup used for position calibration. On the left, we can see the tungsten collimator with a space left for the ^{137}Cs source (not present when not actively gathering data due to radiation protection considerations). In the centre, the $CeBr_3$ scintillator wrapped in Teflon and the associated electronics. On the right, the X-Y motorised translation table (in black) used for scanning the surface of the scintillator.

important to have a comprehensive calibration campaign and robust models of the detector response.

4. Calorimeter prototype calibration results

4.1. Calorimeter energy calibration

We have performed a calibration campaign of a prototype calorimeter for the ComPol mission. The prototype represents a miniaturised detector to be flown on the ISS in 2023 as a technological demonstrator for an in-orbit verification (IOV). The calorimeter is a $CeBr_3$ scintillator coupled to a 6x6 S14161 silicon photomultiplier (SiPM) array from Hamamatsu Photonics. Additionally, we will install a plastic scintillator, covering one side of the $CeBr_3$ read-out by 2 single pixel S14160 Hamamatsu SiPMs. The plastic scintillator is designed to act as a veto-shield for the final ComPol payload and surround the whole $CeBr_3$ but due to space constraints and limited readout channels, we have decided to have just one face covered by the veto for the IOV mission. The front-end electronics consists of a 32 channel EASIROC ASIC readout by 12 bit/10MSPs ADCs and a Zynq SOC (to be replaced for the actual mission by a custom on-board computer).

The detector design has been aided by Geant4 simulations in order to define the best compromise between position reconstruction performance and detector efficiency. Due to the very small distance between the two detector planes, position reconstruction is critical, thus, we set a 2 mm resolution objective which is similar performance to equivalent detectors [21]. Since the shape of the scintillator is dictated by the size of the SiPM array, which is 25.4 mm, we have simulated different thicknesses for the crystal, with the 15 mm one striking the balance between efficiency and position reconstruction.

The instrument has been designed to fit in a 1U (10x10x10 cm) of a CubeSat. Given the space restriction and the number of channels incompatibility between the SiPM array and the ASIC, we were forced to leave floating the four corner pixels and connect 2 pixels together on one channel, leaving one channel for the readout of the plastic scintillator. Despite this limitation, performance has been shown not to be critically affected.

Source	Energy (keV)
^{57}Co	122
^{137}Cs	32
	661.6
^{133}Ba	81
	356
^{60}Co	1173.2
	1332.5
^{22}Na	511
	1274.5

Table 1: Sources used for energy calibration.

Preliminary energy calibration has been executed with 5 radioactive sources at Saclay, presented in table 1. Given that the EASIROC ASIC has two analogue amplification channels with a factor 10 gain difference between them, we have calibrated

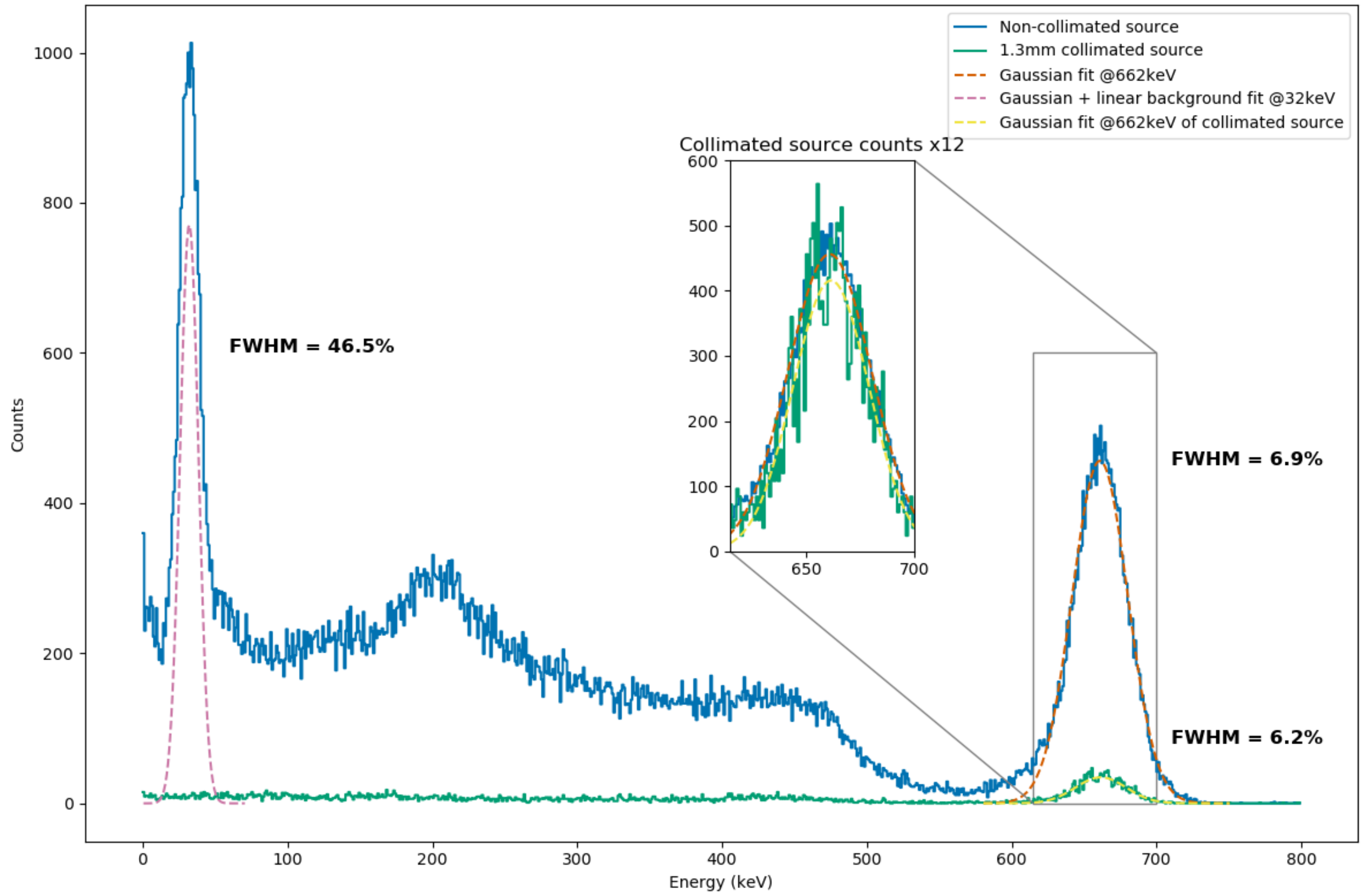

Figure 4: A ^{137}Cs source acquisition with the low-gain channel of the ASIC. The 32 keV and 661.6 keV lines are fitted with a gaussian and have a 46.5% and 6.9% FWHM resolution respectively. The zoomed in frame shows the same data but the collimated measurement counts are multiplied by 12 for easier comparison.

both of them. We will refer to the two channels as high-gain and low-gain respectively in the suite of this article.

We have obtained good linearity in the high-gain channel for energies < 200 keV and in the low-gain channel for energies up to 1.3 MeV, which is the highest energy source we had available at the lab. The calibration curves are shown in figure 5. Theoretically, the upper energy threshold should be around 4 MeV, although it might still be possible to exploit the data in the non-linear region. Since the monolithic scintillator is read out by a matrix of SiPMs, spectra are obtained from summing over all the channels. Thus, the saturation we see at higher energies has been proven to be an effect of individual pixel saturation, where most of the light is incident on one pixel, and not an artefact of the high-gain chain of the ASIC.

The detector has a low energy threshold of 15 keV and a FWHM resolution of 6.9% @662 keV and 46.5% @32 keV. The resolution can be furthermore improved by reconstructing the position of interaction in the crystal and applying a corrective factor. This is possible due to the non-uniform collection of light inside the scintillator and can be seen most prominently at the edges of the crystal. To illustrate this, Figure 4 includes two measurements of a ^{137}Cs source with

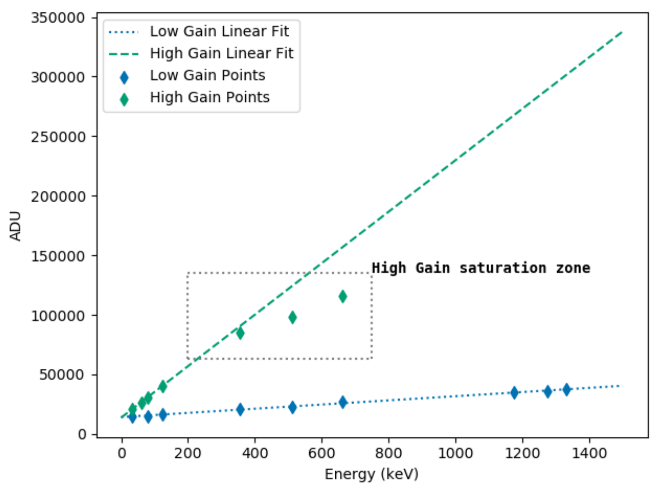

Figure 5: Calorimeter calibration curves in the High/Low Gain channels of EASIROC chip.

and without a collimator. The collimated source measurement has a better energy resolution, 6.2% @662 keV, since the light collection is constant in this case. It is also important to note that the energy resolution has been negatively affected by a couple of anomalies during the calibration campaign. First of all, a firmware bug caused us to lose all the data on the last channel of the ASIC. Secondly, the second to last channel has been damaged before the calibration campaign. The loss of two pixels plus the four corner pixels that are not connected has an impact on the measured energy resolution. The positive conclusion from this is that even with 1/6th of the pixels not responding, the performance has not been affected in a critical manner. Furthermore, position reconstruction performance is still very good, to be detailed in the following section.

4.2. Calorimeter position calibration

We have also performed a position reconstruction calibration campaign. The same setup as described in [21] has been used for calibration, see figure 3. The detector is installed on a X-Y motorised translation bench and a ^{137}Cs source is positioned behind a 10 cm thick tungsten collimator with a 1.3 mm opening. The translation bench is then used to scan the whole surface of the detector with half pixel steps (2 mm), which amounts to 11 points per axis and 121 total calibration positions. The resulting data was then used to determine the position reconstruction performance of the calorimeter. We use the standard deviation of the the reconstructed X,Y position with regards to the known position to evaluate the performance of the reconstruction method $\overline{\sigma}_{XY}$, this is defined as follows (see [21]):

$$\overline{\sigma}_{XY} = \sqrt{\frac{1}{N}\sum_{p} N_p \sigma^2_{XY,p}} \tag{3}$$

with

$$\sigma_{XY,p} = \sqrt{\frac{1}{N_p}\sum_{i=1}^{N_p}[(x_p - x_i^{rec})^2 + (y_p - y_i^{rec})^2]} \tag{4}$$

where N is the total number of events, N_p is the number of events at position p, x_p, y_p are the coordinates of position p and x_i^{rec}, y_i^{rec} are the reconstructed position coordinates.

Two methods were used to analyse the data:

- Centroid calculation of 3-brightest pixels. The advantage of this method is in its simplicity, fast computation time and the capability to do it on-board the satellite. It does, however, lack in performance as evidenced by the error calculation in figure 6. It is also very sensible to broken pixels and generates a non-continuous distribution of calculated positions.

- Using a Neural Network (NN) [22, 23]. This method has been successfully applied to our detector with good results. Contrary to the centroid calculation, the NN reconstruction algorithm is not affected by the missing channels in the data. We have divided the calibration data into 3 datasets in order to validate this method. The first dataset of 50 events per mechanical position is used to train the model. A second dataset of the following 100 events/position is used to validate the reconstruction performance and compare it to the training dataset so that the model does not over-specialise. Finally, the rest of the events are used to reconstruct the position of interaction and estimate the performance of the method.

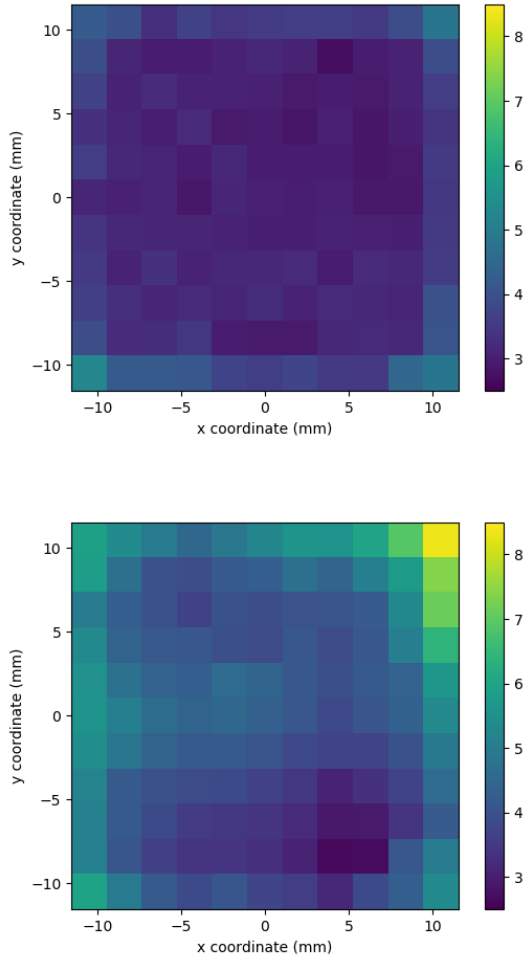

Figure 6: RMS error, in mm, of reconstructed position with a Neural Network model (*top*) and by centroid calculation (*bottom*). Each square represents the RMS error for a given mechanical position used during calibration.

Table 2 summarizes the performance obtained with the two methods of position reconstruction. We have calculated three separate values for the position reconstruction in the corners, on the edges and in the bulk of the scintillator in order to illustrate the degraded performance near the edge of the scintillator, which can also be seen in Figure 6.

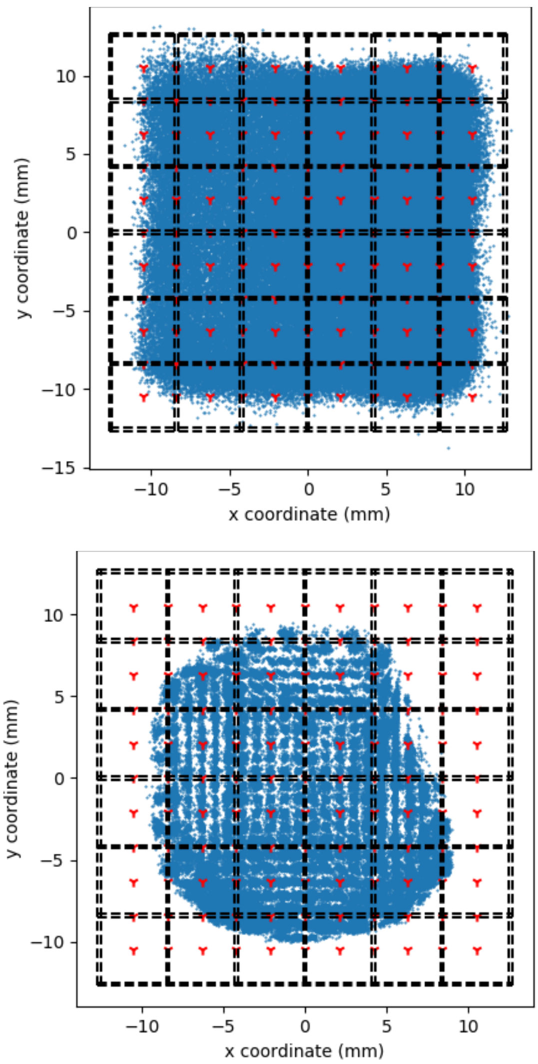

Figure 7: Reconstructed positions of interaction, with a Neural Network model (*top*) and by centroid calculation (*bottom*). The SiPM array pixels are represented by the black dashed lines, the reconstructed positions - by the blue points, and the true positions - by the red triangle points.

Position	σ_{XY}	
	NN	Centroid
Body	3.08 ± 0.13	4.04 ± 0.56
Edges	3.69 ± 0.28	5.1 ± 0.96
Corners	4.78 ± 0.38	6.35 ± 1.15
All	3.32 ± 0.44	4.43 ± 0.94

Table 2: Calculated RMS error values for the two position reconstruction methods.

Figure 7 shows all the reconstructed positions from the dataset. As mentioned earlier, centroid calculation is very sensible to missing data, which is evidenced by the lack of reconstructions in the corners ,because the corner pixels are not connected, and in the upper right part of the SiPM matrix, where channel 31 of the ASIC was broken and channel 32 was missing data.

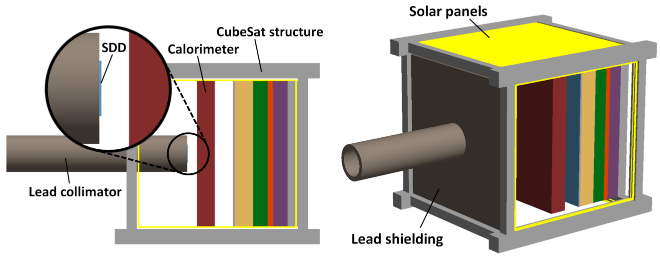

(a) Side view with zoom on SDD (b) Perspective view

Figure 8: Visualisation of the simulated geometry. The set-up is simplified from three CubeSat units down to one unit (10x10x11.35 cm^3) to reduce the simulation time. It consists of the Silicon Drift Detector (SDD), the $CeBr_3$ calorimeter, a lead collimator and shielding plate, the aluminium CubeSat structure, solar panels on all four sides (indicated by yellow lines), and a block of different material layers behind the detector system which account for the material distribution in the whole CubeSat.

5. Sensitivity study

A dedicated sensitivity study was performed for the ComPol project to predict the Minimum Detectable Polarisation (MDP) of the final instrument using calibration derived performances of the detectors. The MDP is a widely used parameter which describes the lowest degree of polarisation measurable on a 99% confidence level [24]. This value strongly depends on the detector geometry and performance. The study described in this section is based on simulations conducted with the Monte Carlo particle simulation software Geant4. The following table summarises a few aspects of the simulation and how they are implemented:

- **Geometry:**
  A simplified satellite geometry is taken into account (see figure 8). This includes the exact dimensions of the detector volumes, a lead collimator and shielding plate in front of the detectors, and the aluminium structure of the satellite. Most of the other components used in the satellite can so far only be estimated approximately. But their preliminary material composition is also implemented as a material block behind the detector system.

- **Simulated physics:**
  For a Geant4 simulation it is necessary to define the physics that are considered (particles, interactions, etc.). For the full picture, the predefined constructors for the Geant4 Physics List are mentioned here:
  - `G4EmLivermorePolarizedPhysics`
  - `G4HadronPhysicsQGSP_BERT_HP`
  - `G4DecayPhysics`
  - `G4RadioactiveDecayPhysics`
  - `G4EmExtraPhysics`

  The first one covers the low energy electromagnetic part, especially important for the signal simulation. The four others are necessary for the background simulation. They cover hadronic processes including cosmogenic activation of the CubeSat materials and the subsequent decays.

- **Spectra:**
  The real X-ray flux of Cygnus X-1 is simulated for the signal simulation (Data from [25]).

  Besides this, all relevant background particles and their energy distributions in a low earth orbit (550km altitude, 85° inclination) are considered for the background simulation. This is on one hand the direct background during the whole orbit, consisting of photons, electrons, positrons, protons, alpha particles, and neutrons (Data from [26]) and on the other hand the cosmogenic activation during fly-throughs through the South Atlantic Anomaly (SAA, Data from [27]).

- **Detector system:**
  The detector system consists of a Silicon Drift Detector (SDD) and a $CeBr_3$ scintillator. The following detector performance used in the simulation is derived from calibration data, as detailed in the previous section.

  SDD characteristics:

  – Module with 32 pixels and a pixel size of 2 mm
  – The position resolution is limited by the pixel size. Each interaction is assumed to be in the centre of the respective pixel.
  – The energy resolution of the SDD is $\sim$ 500eV FWHM @ 6 keV
  – Lower energy threshold: 1 keV

  $CeBr_3$ scintillator characteristics:

  – Crystal size: 80x80x10 mm^3
  – $\sigma_X = \sigma_Y = 2.3$ mm gaussian position resolution [1]
  – See sections above for the energy resolution
  – Lower energy threshold: 15 keV

The simulation data is analysed in the same way as real data. Thanks to the event wise measured scattering position, absorption position and the respective energies it is possible to reconstruct the scatter angle θ in two different ways (geometrically and via the energies using the Compton formula [20]). Selecting only events where both reconstructed scatter angles match, is a very powerful cut that allows to exclude more than 97 % background events that created a time coincidence between the two detectors. This reduction of the background rate reflects in an improvement of the signal to noise ratio for the polarisation detection from approx. 15 to 36. A second event selection stage further improves the sensitivity on the polarisation. For this, the Compton events with small scatter angles get excluded. Since the polarisation dependence vanishes for small scatter angles, these events would appear as a unpolarised flat background [28]. Figure 9 shows a histogram of the azimuthal scatter angle ϕ of all remaining events for a 100% polarised beam. This distribution is described by the following equation:

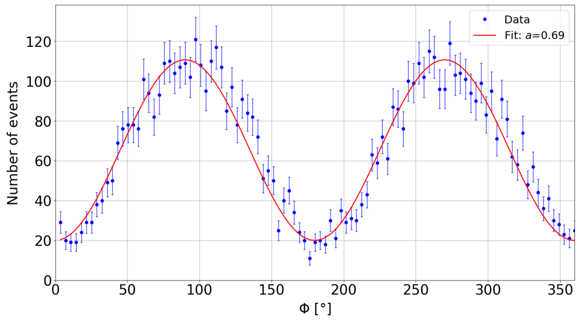

Figure 9: Histogram for the signal simulation of the azimuthal scatter angle ϕ after the event selection for a 100% polarised beam. The modulation amplitude is the imprint of the degree polarisation, and the positions of the minima reflect the initial polarisation plane.

$$f_P(\Phi) = C \cdot [1 + a\cos(2(\Phi - \psi))] \quad (5)$$

Fitting this curve to the data yields the resulting modulation amplitude a. In the case of a 100% polarised beam, we define:

$$\mu_{100} = a \quad (6)$$

This is an instrument dependent parameter that describes the maximum possible modulation. Together with values of the signal rate R_S and background rate R_B:

$$R_S = 0.30 \cdot 10^{-3}\text{cps}, \qquad R_B = 1.16 \cdot 10^{-3}\text{cps} \quad (7)$$

one can derive the MDP [29]:

$$\text{MDP} = \frac{4.29}{\mu_{100} \cdot R_S}\left(\frac{R_S + R_B}{T}\right)^{1/2} \quad (8)$$

This results in an MDP of 19.5% after 6 months observation time T.

Discussion of the result

The resulting MDP is reasonable and a success given the small effective detector area (~1 cm^2). It shows that it is possible to construct Nano-Sat missions capable of measuring polarisation data in the gamma-ray range. The biggest challenge ahead is to further optimise the system despite strong limitations in size, weight and power consumption. To do so there are still options left e.g. optimising the shielding strategy by using a graded shielding or an active veto system, optimising the geometrical detector arrangement (e.g. distance between SDD and $CeBr_3$) and also optimising the detectors themselves as already mentioned for the $CeBr_3$ in the section before. In addition to that, the conducted background study should be quite conservative since it was made for the worst case orbit (polar orbit).

[1] $\sigma_{XY} = \sqrt{\sigma_X{}^2 + \sigma_Y{}^2}$

6. Conclusion and outlook

We have presented the imaging and spectral performance of a monolithic calorimeter designed for use in a Compton Polarimeter. Despite its small size and limited read-out channels, the position of interaction reconstruction is comparable with bigger equivalent systems [21]. This is a very good result given the short design and implementation time, which was 1 year. It also shows the capacity for a rapid development cycle for space instruments on-board nano-satellites. Furthermore, simulation studies of the ComPol payload show promising performance for a 1-year mission. For the future, this design could be optimised further and used for observations of other astrophysical sources.

A more thorough calibration campaign of the IOV model of the instrument is planned for the end of 2022. Whilst this paper presents only the calorimeter performance, we plan on using the whole polarimeter, i.e. calorimeter + SDD working in coincidence, for a beam-test campaign at the LARIX facility at University of Ferrara. We are currently working on the final version for the IOV mission which should be launched to the ISS in 2023 and a planned CubeSat mission for the end of 2025, thus exemplifying the highly dynamic world of nano-satellite design. This comes at an opportune moment, with dedicated polarimetry missions being planned, which could hopefully lead to joint observations of gamma-ray sources.

7. Acknowledgments

This research is supported by the Excellence Cluster ORIGINS which is funded by the Deutsche Forschungsgemeinschaft (DFG, German Research Foundation) under Germany's Excellence Strategy - EXC-2094-390783311

References

[1] Armen Poghosyan and Alessandro Golkar, CubeSat evolution: Analyzing CubeSat capabilities for conducting science missions, Progress in Aerospace Sciences 88 (2017) 59–83.

[2] Stéphane Callier, Christophe Dela Taille, Gisèle Martin-Chassard, and Ludovic Raux, Easiroc, an easy & versatile readout device for sipm, Physics Procedia 37 (2012) 1569–1576, proceedings of the 2nd International Conference on Technology and Instrumentation in Particle Physics (TIPP 2011).
URL `https://www.sciencedirect.com/science/article/pii/S1875389212018688`

[3] Tanmoy Chattopadhyay, Hard X-ray polarimetry—an overview of the method, science drivers, and recent findings, Journal of Astrophysics and Astronomy 42 (2) (2021) 106. arXiv:2104.05244, doi:10.1007/s12036-021-09769-5.

[4] Astronomical Polarisation from the Infrared to Gamma Rays, Vol. 460 of Astrophysics and Space Science Library.

[5] Matthias Beilicke, F. Kislat, A. Zajczyk, et al., Design and performance of the x-ray polarimeter x-calibur (2014).
URL `https://arxiv.org/abs/1412.6457`

[6] M. Chauvin, M. Jackson, T. Kawano, et al., Optimising a balloon-borne polarimeter in the hard X-ray domain: From the PoGOLite Pathfinder to PoGO+, Astroparticle Physics 82 (2016) 99–107.

[7] Y. Kishimoto, S. Gunji, Y. Ishigaki, et al., Basic performance of phenex: A polarimeter for high energy x rays, IEEE Transactions on Nuclear Science 54 (3) (2007) 561–566.

[8] S. Gunji, Y. Kishimoto, H. Sakurai, et al., The PHENEX experiment result, in: Polarimetry days in Rome: Crab status, theory and prospects, 2008, p. 5.

[9] P. Bloser, T. Sharma, J. Legere, et al., The Advanced Scintillator Compton Telescope (ASCOT), memsai 90 (2019) 232.

[10] Nicole Duncan, P. Saint-Hilaire, A. Y. Shih, et al., First flight of the Gamma-Ray Imager/Polarimeter for Solar flares (GRIPS) instrument, in: Jan-Willem A. den Herder, Tadayuki Takahashi, and Marshall Bautz (Eds.), Space Telescopes and Instrumentation 2016: Ultraviolet to Gamma Ray, Vol. 9905 of Society of Photo-Optical Instrumentation Engineers (SPIE) Conference Series, 2016, p. 99052Q.

[11] P. F. Bloser, J. S. Legere, J. R. Macri, et al., GRAPE - A Balloon-Borne Gamma-Ray Polarimeter Experiment, Chinese Journal of Astronomy and Astrophysics Supplement 6 (S1) (2006) 393–397.

[12] M. Forot, P. Laurent, I. A. Grenier, et al., Polarization of the Crab Pulsar and Nebula as Observed by the INTEGRAL/IBIS Telescope, apjl 688 (1) (2008) L29.

[13] P. Laurent, J. Rodriguez, J. Wilms, et al., Polarized Gamma-Ray Emission from the Galactic Black Hole Cygnus X-1, Science 332 (6028) (2011) 438.

[14] S. V. Vadawale, T. Chattopadhyay, A. R. Rao, et al., Hard X-ray polarimetry with Astrosat-CZTI, aap 578 (2015) A73.

[15] Daisuke Yonetoku, Toshio Murakami, Shuichi Gunji, et al., Gamma-Ray Burst Polarimeter (GAP) aboard the Small Solar Power Sail Demonstrator IKAROS, Publications of the Astronomical Society of Japan 63 (3) (2011) 625–638. arXiv:https://academic.oup.com/pasj/article-pdf/63/3/625/17442302/pasj63-0625.pdf.
URL `https://doi.org/10.1093/pasj/63.3.625`

[16] M. Kole, T. W. Bao, T. Batsch, et al., Polar: Final calibration and in-flight performance of a dedicated grb polarimeter (2016).
URL `https://arxiv.org/abs/1612.04098`

[17] J. Tomsick and COSI Collaboration, The Compton Spectrometer and Imager Project for MeV Astronomy, in: 37th International Cosmic Ray Conference. 12-23 July 2021. Berlin, 2022, p. 652.

[18] Nasa selects gamma-ray telescope to chart milky way evolution, `https://www.nasa.gov/press-release/nasa-selects-gamma-ray-telesc`

[19] Carolyn A. Kierans, Steven E. Boggs, Jeng-Lun Chiu, et al., The 2016 Super Pressure Balloon flight of the Compton Spectrometer and Imager, arXiv e-prints (Jan. 2017). arXiv:1701.05558.

[20] Arthur H. Compton, A Quantum Theory of the Scattering of X-rays by Light Elements, Physical Review 21 (5) (1923) 483–502.

[21] Adrien Laviron, Valentin Gourlaouen, Clarisse Hamadache, et al., Optimization of cebr3 position-sensitive calorimeter module, Nuclear Instruments and Methods in Physics Research Section A: Accelerators, Spectrometers, Detectors and Associated Equipment 1007 (2021) 165379.
URL `https://www.sciencedirect.com/science/article/pii/S016890022`

[22] Adrien Laviron, Développement d'un prototype de télescope compton et astronomie gamma, Ph.D. thesis, thèse de doctorat dirigée par Hamadache, Clarisse et Tatischeff, Vincent Astrophysique nucléaire et nucléosynthèse université Paris-Saclay 2022 (2022).
URL `http://www.theses.fr/2022UPASP048`

[23] Aleksandar Gostojić (Gostojic), Développement d'un télescope comton avec un calorimètre imageur 3d pour l'astronomie gamma, Ph.D. thesis, thèse de doctorat dirigée par Tatischeff, Vincent Astrophysique nucléaire et nucléosynthèse Université Paris-Saclay (ComUE) 2016 (2016).
URL `http://www.theses.fr/2016SACLS136`

[24] M. C. Weisskopf, X-ray polarimetry: historical remarks and other considerations, Cambridge Contemporary Astrophysics, Cambridge University Press, 2010, p. 1–8.

[25] F. Cangemi and J. others Rodriguez, High energy spectral study of the black hole Cygnus X-1 with INTEGRAL (2018).
URL `http://arxiv.org/abs/arXiv:1810.12049`

[26] P. Cumani, M. Hernanz, et al., Background for a gamma-ray satellite on a low-Earth orbit, Experimental Astronomy 47 (3) (2019) 273–302.

[27] Messios N. De Donder, E. et al., SPENVIS – the space environment information system (version 4.6.10) (2022).
URL `www.spenvis.oma.be`

[28] F. Muleri and R. Campana, Sensitivity of stacked imaging detectors to hard X-ray polarization, The Astrophysical Journal 751 (2) (2012) 88.

[29] Martin C Weisskopf, Ronald F Elsner, and Stephen L O'Dell, On understanding the figures of merit for detection and measurement of x-ray polarization, in: Space Telescopes and Instrumentation 2010: Ultraviolet to Gamma Ray, Vol. 7732, SPIE, 2010, pp. 98–102.